

ARTICLE

Open Access

Visible-light photocatalysis by carbon-nano-onion-functionalized ZnO tetrapods: degradation of 2,4-dinitrophenol and a plant-model-based ecological assessment

Seung Jun Park¹, Gouri Sankar Das¹, Fabian Schütt², Rainer Adelung², Yogendra Kumar Mishra², Kumud Malika Tripathi¹ and TaeYoung Kim¹

Abstract

The visible-light-induced photocatalytic performance of a three-dimensional (3D) hybrid composite based on carbon nano-onion (CNO)-functionalized zinc-oxide tetrapods (T-ZnO) was investigated to study the photocatalytic degradation of 2,4-dinitrophenol (DNP). The hybrid CNO-functionalized T-ZnO 3D composite was successfully developed via a facile one-step process. The CNOs, synthesized via a green route from flaxseed oil, were decorated on the surface of T-ZnO via chemical mixing. Such a hybrid composite allows for the complete optimization of the T-ZnO/CNO interface to enhance visible-light harvesting, contributing to effective visible-light-induced photocatalysis. The enhanced photocatalytic performance of the T-ZnO-CNO 3D composite is attributed to the strong synergistic effects obtained by the unique cumulative intrinsic properties of CNOs and the 3D architecture of T-ZnO, which lead to exceptional charge transfer and separation. A reaction mechanism for the degradation of DNP is proposed based on a bandgap analysis and trapping experiments. Furthermore, the photocatalyst maintains a favorable reusability during consecutive cycling experiments. The ecological assessment of the photocatalytic process was performed via the germination of common gram seeds (*Cicer arietinum*) and reveals the low toxicity and environmental safety of the synthesized hybrid 3D composite. The observations confirm that the synthesized hybrid 3D composite facilitates wastewater decontamination using photocatalytic technology and highlights the broad implications of designing multifunctional materials for various advanced applications.

Introduction

Ever-increasing global demand and environmentally unfriendly human activities are continuously drawing the attention of the research community towards contaminated water treatments and their long-term sustainability for the future¹. Wastewater is mostly produced from the emissions of a wide range of organic

contaminants, which are widespread in industrial, agricultural, and household applications^{2,3}. The removal of organic pollutants from wastewater is currently a primary challenge to circumvent the world's water crisis, owing to their high resistance to biodegradation⁴. 2,4-Dinitrophenol (DNP) has been known as a priority pollutant because of its mutagenic and carcinogenic nature and bioaccumulation⁵. DNP is widely utilized in the production of diverse industrial products, chemicals, wood preservatives, pesticides, paints, pharmaceuticals, dyes, textiles, and petrochemicals⁶. Superfluous DNP largely exists in industrial effluents, soil, and aquatic environments⁵. The major risks associated with DNP

Correspondence: TaeYoung Kim (taeykim@gachon.ac.kr) or Kumud Malika Tripathi (kumud20010@gmail.com)

¹Department of Bionanotechnology, Gachon University, 1342 Seongnam-daero, Sujeong-gu, Seongnam-si, Gyeonggi-do 13120, South Korea

²Functional Nanomaterials, Institute for Materials Science, Kiel University, Kaiserstr. 2, D-24143 Kiel, Germany

© The Author(s) 2019



Open Access This article is licensed under a Creative Commons Attribution 4.0 International License, which permits use, sharing, adaptation, distribution and reproduction in any medium or format, as long as you give appropriate credit to the original author(s) and the source, provide a link to the Creative Commons license, and indicate if changes were made. The images or other third party material in this article are included in the article's Creative Commons license, unless indicated otherwise in a credit line to the material. If material is not included in the article's Creative Commons license and your intended use is not permitted by statutory regulation or exceeds the permitted use, you will need to obtain permission directly from the copyright holder. To view a copy of this license, visit <http://creativecommons.org/licenses/by/4.0/>.

contamination are its high aqueous solubility, bioaccumulation, high toxicity, and mutagenic and genotoxic nature, which endanger the environment and human health². Moreover, DNP can significantly inhibit biological cell growth, even at a concentration of 1 ppm (part per million)⁵. Therefore, the removal of DNP from water bodies is imperative and has been the subject of intense research. The removal of DNP is complex owing to its high stability and resistance to biodegradation in addition to concerns about the generation of toxic intermediates. The current technology for the removal of organic contaminants is dependent on adsorption, and it has limitations such as poor efficiency, time-consuming procedures, and requirements of large investments^{7,8}. However, the ecological assessment of water after the removal of DNP should also be addressed to achieve a supportable ecosystem. Thus, a facile, sustainable, and cost-effective method is required for the effective removal of organic contaminants from water.

Current pursuits for a sustainable resolution to energy and environmental issues have pushed the scientific community towards the development of photocatalysts^{9–11}. Photocatalysis offers advantages such as the utilization of inexhaustible and clean solar energy, high efficiencies, and the negligible generation of hazardous byproducts¹². Photocatalysis has a wide range of applications in environment remediation and material science. The desirable characteristics of photocatalysts are their large active surface area, high charge-separation efficiency, visible-light absorption capacity, and long-term photostability¹³. In this regard, three-dimensionally (3D) structured zinc oxide (ZnO) has been recognized as a remarkable candidate for such applications owing to its advantageous features^{14–16}. The crystalline nature of ZnO as well as its many excellent properties allows for the fast generation of electron–hole pairs when exposed to light¹⁵. However, ZnO tetrapods (T-ZnO) suffer from low activity in visible light owing to a wide bandgap of ~ 3.3 eV and the ready recombination of charge carriers¹⁷. In addition, the visible-light harvesting efficiency of ZnO is relatively low, which restricts its practical utilization¹⁷. Diverse strategies are currently being employed to overcome the aforementioned shortcomings and enhance visible-light-driven photocatalysis efficiency, and the fabrication of composites has aroused substantial interest^{18–20}. However, to date, the overall photocatalytic efficiency of ZnO-based composite materials in the visible-light region remains too low for commercial applicability. Hence, it is exigent to develop a highly efficient visible-light-sensitive ZnO composite for the optimum utilization of visible-light energy.

Numerous studies have suggested that composite materials made of semiconductor nanostructures and nanocarbons are suitable to achieving visible-light-driven

photocatalysis and a tunable bandgap structure^{21–23}. Owing to the presence of abundant, free-flowing sp^2 -hybridized π electrons and photoinduced-electron transfer properties, nanocarbons have improved the harvesting of light energy in the visible region and have also enhanced the photocatalytic performance of semiconductor nanostructures^{24,25}. Moreover, the interface between hybrid materials significantly affects the response of the photocatalyst to light^{26,27}. Surface energy traps generated by interfacial defects hinder electron transfer, owing to weak interfacial interactions, and hence increase charge trapping and recombination^{25,26}. Therefore, better interfacial interactions are crucial to improve the response to light. In this context, carbon nano-onions (CNOs) have considerable potential among other nanocarbons, owing to their unique porous onion-like morphology, large accessible external surface area, high electrical conductivity, biocompatibility, and chemical stability²⁸. CNOs consist of stacked fullerene shells in a quasi-spherical arrangement, ordered in the form of concentric graphitic layers^{29,30}. CNOs have attracted much attention in energy storage and conversion, lubricant additives, catalyst supports, and biomedical applications^{31–34}. However, research on the photocatalytic activity and photocatalytic performance of CNOs and their composites remains limited^{35,36}. CNOs provide abundant active sites for photocatalytic reactions owing to the almost perfect graphitic network, high active surface area, absence of inner particle porosity, and high degree of curvature³³. Moreover, CNOs have considerable potential to act as a trapping center to quench the recombination of electron-hole pairs. In addition, the effects of decorating CNOs on the surface of T-ZnO or at the interphase as well as their influence on bandgap structures have not yet been studied. Furthermore, CNO-sensitized T-ZnO presents distinct advantages such as high stability, enhanced photocatalytic activity, hydrophobicity, a facile synthesis, and low cost, thus, facilitating possible commercialization in real technologies. The decoration of smaller CNOs on the surface of T-ZnO can provide more active sites and accelerate the charge separation response.

A crucial issue associated with nanomaterial-based photocatalysis is the sustainability of the overall process. Current research on photocatalytic water remediation is focused on the development of sustainable materials and the improvement in the degradation efficiency towards targeted pollutants, but it does not include the elimination of possible risk of environmental assessment^{37,38}. Even after the complete degradation of organic pollutants, acute toxicity has been observed owing to the generation of toxic byproducts⁴. Therefore, the determination of the concentration of DNP in treated water may not be sufficient, and an accurate environmental risk assessment is highly desirable to evaluate the overall efficiency of

wastewater treatments. The safety of water must be carefully studied before the practical utilization of treated water. In this context, the environmental applicability of treated water has been evaluated through the germination of common gram seeds (*Cicer arietinum*) before and after the photocatalytic degradation of DNP using a T-ZnO-CNO 3D hybrid composite. Gram plants have emerged as excellent model plants, and they are valuable in assessing environmental risks, with a focus on germination and growth to obtain information on the toxicity of water.

The T-ZnO-CNO hybrid composite was fabricated via a simple one-step process for enhanced photocatalytic activity in the visible-light region. The 3D architecture of T-ZnO facilitates the transport of photogenerated carriers owing to a direct electrical pathway. The decoration of CNOs on T-ZnO enhances visible-light harvesting and increases the number of active surface sites for photocatalysis. The photocatalytic performance of the T-ZnO-CNO 3D hybrid composite was evaluated via the degradation of DNP under visible-light irradiation. The T-ZnO-CNO hybrid composite was used for the effective photocatalytic degradation of DNP, which was assessed using the enhanced seed germination of gram plants along with enhanced shoot length. The efficient photocatalytic degradation is attributed to the effective recombination of the photogenerated charge carriers in the CNOs. Moreover, the presented tetrapod-based composite can be easily recycled owing to its hydrophobic nature. The reactive species involved in the photocatalytic degradation of DNP were investigated via radical trapping experiments, and accordingly, a reasonable photocatalytic mechanism is proposed.

Experimental

Materials

All the purchased chemicals were of analytical grade and used as obtained. DNP was purchased from Sigma Aldrich (Korea) and was adopted as a target contaminant to explore the photocatalytic behavior of the synthesized materials. Tert-butanol (t-BA), disodium ethylenediaminetetraacetate (Na_2EDTA) and p-benzoquinone (P-BZQ) were purchased from Sigma Aldrich. The water utilized throughout the experimental process was deionized water (DI water) unless stated otherwise. Common gram (*Cicer arietinum*) seeds were procured from a local market in Korea.

Measurement

The morphology and structure of the synthesized materials were identified using a scanning electron microscope (SEM, JEOL Model: JSM-7500F, Japan) operated at 20 kV and a transmission electron microscope (TEM, FEI Tecnai G2 Model: F30, USA; high-resolution TEM (HRTEM)) operated at 300 kV. Powder X-ray diffraction (XRD) data

were collected using a Rigaku RINT-2000, Japan, with $\text{Cu K}\alpha$ radiation at a scanning rate of 1° min^{-1} . Solid-state Fourier transform infrared (FTIR) spectral analyses were performed using a BRUKER Vector22 IR spectrometer, Germany. The UV-visible spectra were obtained using a Shimadzu UV 2550 spectrophotometer. The optical properties were analyzed using UV-vis diffuse reflectance spectra (DRS) acquired with a PerkinElmer, UK, UV-vis spectrometer with BaSO_4 as the internal reflectance standard. The surface elemental composition and bonding environment were evaluated using X-ray photoelectron spectroscopy (XPS) with an Axis Supra (Kratos, UK) system having an Al $\text{K}\alpha$ X-ray source. The Brunauer-Emmett-Teller (BET) surface area was analyzed by the N_2 adsorption-desorption isotherms measured at 77 K on a BELSORP-max (Microtrac BEL Corp., Japan).

Synthesis of CNOs and ZnO tetrapods

CNOs were synthesized by adopting a previously developed, traditional wick pyrolysis technique using flaxseed oil as the precursor^{35,39,40}. In particular, flaxseed oil was pyrolyzed in an earthen pot using a cotton wick under stable air conditions. The soot was collected over the surface of a clean inverted glass beaker from the top of the flame. Subsequently, 5 g of the as-synthesized soot was heated at 550°C for 1 h in a muffle furnace to remove amorphous carbon or unburnt oil. A size separation was performed to obtain uniformly distributed CNOs. After heating, the CNOs were dispersed in ethanol via sonication for 10 min and were filtered using a $0.2\text{-}\mu\text{m}$ -thick membrane filter. The obtained CNOs were hydrophobic in nature and could be dispersed in water or organic solvents via sonication. The micro- and nanoscale T-ZnO, as a scaffold material for the deposition of CNOs, was synthesized by adopting a recently introduced flame transport synthetic technique with further modification⁴¹⁻⁴³. A simple Zn wire (99.9% purity, 12–15 g) was placed in a preheated furnace (950°C) in an inert atmosphere. Subsequently, pressured air was flowed through the furnace for rapid ZnO oxidation, leading to the synthesis of free-standing T-ZnO powder in gram-scale yields.

Synthesis of the hybrid T-ZnO-CNO 3D hybrid composite

An aqueous dispersion of CNOs was prepared via sonication at 25°C . The CNOs were mixed in water at a concentration of 1 mg mL^{-1} (30 mg CNOs in 30 mL water) and sonicated for 20 min, resulting in a black viscous solution without visible precipitation. Subsequently, 30 mg T-ZnO was added to the above-prepared solution and continuously stirred for 12 h under ambient conditions. The resultant suspension was filtered, repeatedly washed with water to remove excess CNOs and dried overnight at 80°C in an oven.

Photocatalytic degradation of DNP

The degradation of DNP in an aqueous solution was performed under ambient conditions to assess the photocatalytic activity of the T-ZnO-CNO under visible-light irradiation. In a typical experiment, 100 mg of the T-ZnO-CNO composite was dispersed in 50 mL of DNP solution (0.1 mM), and prior to irradiation, the solution was stirred in the dark for 40 min (to achieve adsorption–desorption equilibrium). This solution was irradiated using a 60 W tungsten bulb, and the distance between the liquid surface and the light source was fixed at 15 cm. Aliquots were collected at a fixed time interval (10 min) and centrifuged at 8000 rpm for 5 min to remove the residual particles. The residual concentration of DNP was monitored using a UV-visible spectrophotometer. The rate constant for the photodegradation of DNP can be expressed using the Langmuir-Hinshelwood equation ($\ln(C/C_0) = -kt$), where k is the reaction rate constant and C_0 and C represent the initial concentration and the concentration at time t , respectively⁴⁴. The activity of the photocatalyst was evaluated based on the degradation rate of DNP.

Assessment of ecotoxicity with *Cicer arietinum* seed germination

The toxicity of the samples after DNP degradation was evaluated by monitoring growth inhibition in the seed germination of common gram (*Cicer arietinum*)^{45,46}. Common gram plant seeds were placed under normal conditions in a dry and sterile place before germination. The surface sterility of the seeds was achieved by soaking them in a 10% sodium hypochlorite solution for 10 min, followed by washing with normal water, and the seeds were subsequently soaked in water for 1 day to promote germination before use⁴⁷. One-day-old sprouted gram seeds were transferred into four Petri dishes lined with cotton containing either DI water, DNP solution, CNO solution, or the DNP solution photo-degraded using the T-ZnO-CNO hybrid composite. These seeds were allowed to further germinate for 10 days, and their germination frequencies (seedling growth, root length, and shoot length) were analyzed after 7 days of germination.

Results and discussion

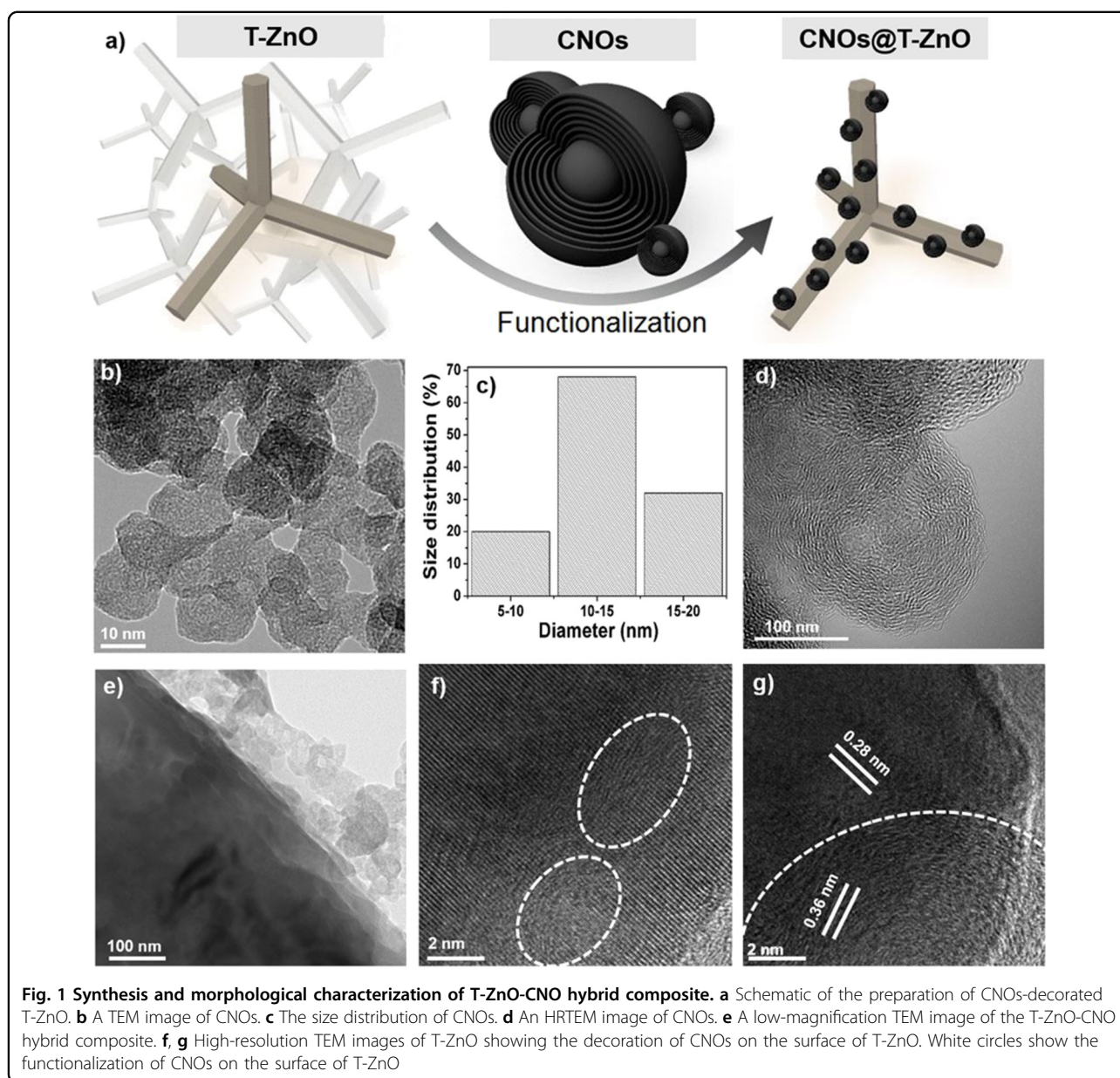
The fabrication strategy for the T-ZnO-CNO hybrid composite is demonstrated in Fig. 1a. Three-dimensional tetrapods were utilized as the backbone for the decoration of the CNOs. The high hydrophobicity and 3D architecture of T-ZnO facilitate the attachment of CNOs on the ZnO arms via hydrophobic–hydrophobic interactions. The difference between the surface energies of T-ZnO and CNOs, associated with the oxygen vacancies of T-ZnO and the surface defects of CNOs, is attributed to the long-range attractive interactions, leading to the

functionalization of smaller CNOs on the flat side faces of T-ZnO^{48,49}. The high degree of overlap between the hydrophobic regions of T-ZnO and CNOs, owing to different shapes, surface defects, and surface areas, leads to the stable attachments of CNOs on the surface of T-ZnO⁴⁸. T-ZnO is not readily suspended in water, but the T-ZnO-CNO hybrid composite can be easily dispersed in water and remains stable overnight. The unreacted T-ZnO was removed from the solution based on differences in solubility. The decoration of CNOs on the surface of ZnO not only enhances the reactive sites for photocatalysis but also facilitates the recovery of the catalysts for practical applications.

Morphological studies of the T-ZnO-CNO hybrid composite

The morphologies of T-ZnO and the T-ZnO-CNO hybrid composite were observed using an SEM and are shown in Fig. S1. The ZnO exhibits a 3D tetrapod-like morphology with a clear and smooth surface (Fig. S1a and b). The length of T-ZnO varies from 10 to 50 μm , and the tip and base diameters are ~ 500 nm and 10 μm , respectively. The typical SEM image of the ZnO-CNO hybrid composite in Fig. S1c shows the decoration of CNOs on the surface of ZnO tetrapods. In contrast with T-ZnO, the T-ZnO-CNO hybrid composite shows no apparent change in the morphology. The detailed high-resolution SEM analysis of the T-ZnO-CNO hybrid composite shown in Fig. S1d reveals the decoration of CNOs on the surface of T-ZnO and the formation of a composite structure.

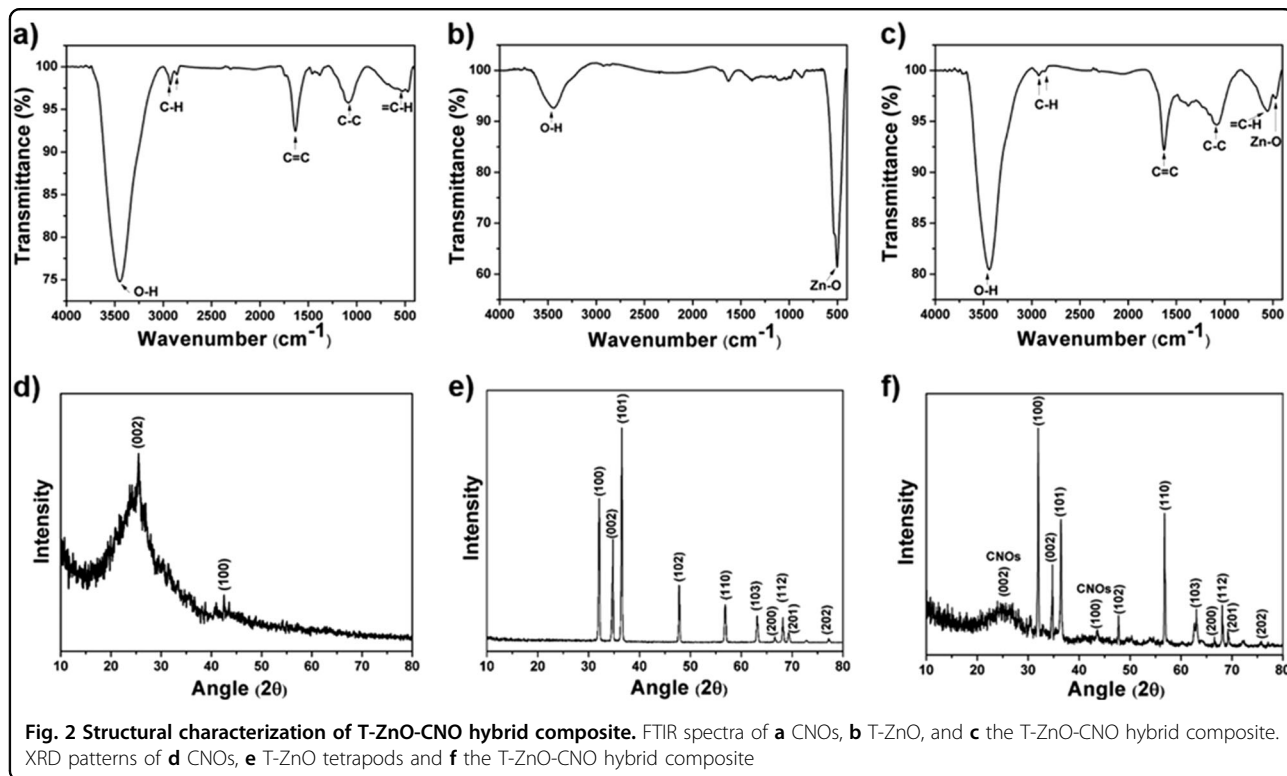
The morphologies of the synthesized CNOs and the T-ZnO-CNO hybrid composite were characterized using TEM and HRTEM analysis. Spherical and well-dispersed CNOs are observed in the low-resolution TEM image (Fig. 1b). The size distribution pattern, as evaluated statistically (Fig. 1c), demonstrates that the CNOs exhibit a relatively narrow size distribution in the range of 5–20 nm, while most of the CNOs are 10–15 nm in diameter. The crystallinity of the CNOs is revealed by the HRTEM image (Fig. 1d), which displays the multiple layers of concentric nanographene shells with a well-defined spherical shape. The low-resolution TEM image of the T-ZnO-CNO hybrid composite shown in Fig. 1e confirms that the CNOs were deposited on the surface of T-ZnO. The HRTEM images confirm the high crystallinity of the T-ZnO-CNO hybrid composite and reveal the attachment of CNOs with concentric graphene layers on the surface and tip of T-ZnO, as marked by white circles (Fig. 1f, g). The distinct lattice fringes observed at 0.28 nm and 0.36 nm are consistent with the ZnO (100)¹⁷ and CNOs (002) facets, respectively (Fig. 1g). The HRTEM results further demonstrate that CNOs are anchored on the surface of T-ZnO, and such a composite structure can utilize the interface between the CNOs and T-ZnO to enhance the photocatalytic performance.



The FTIR spectra of the CNOs, T-ZnO, and T-ZnO-CNO hybrid composite are shown in Fig. 2a–c. The FTIR spectrum of the CNOs exhibits the characteristic peaks of graphitic carbon. The doublet at $\sim 2922\text{ cm}^{-1}$, strong peak at $\sim 1633\text{ cm}^{-1}$, medium band at $\sim 1084\text{ cm}^{-1}$, and broad band at $\sim 533\text{ cm}^{-1}$ are attributed to alkyl C–H stretching, C=C stretching, C–C stretching, and =C–H bending vibrations, respectively^{37,50}. The broad peak centered at 3449 cm^{-1} is attributed to the surface hydroxyl functional groups and chemisorbed water^{35,51}. The FTIR spectrum of T-ZnO exhibits a characteristic broad peak centered at 3449 cm^{-1} owing to O–H stretching vibrations (Fig. 2b)⁵. The strong peak at 503 cm^{-1} is attributed to Zn–O stretching vibrations⁵. The FTIR spectrum of the T-ZnO-

CNO hybrid composite (Fig. 2c) presents most of the characteristic peaks of the CNOs and ZnO with some shifts in the peak positions attributed to the strong interface between the CNOs and T-ZnO. These peaks include O–H (broad band), –C–H (doublet), C=C (strong), C–C stretching, =C–H bending, and Zn–O stretching vibrations at $\sim 3438\text{ cm}^{-1}$, $\sim 2932\text{ cm}^{-1}$, $\sim 1622\text{ cm}^{-1}$, $\sim 1074\text{ cm}^{-1}$, $\sim 557\text{ cm}^{-1}$, and $\sim 475\text{ cm}^{-1}$, respectively.

XRD patterns were obtained to examine the composition and crystallinity of the pure T-ZnO, CNOs, and T-ZnO-CNO hybrid composite. Figure 2d–f show that both CNOs and T-ZnO possess a crystalline nature. The XRD pattern of CNOs in Fig. 2d, shows two diffraction peaks at



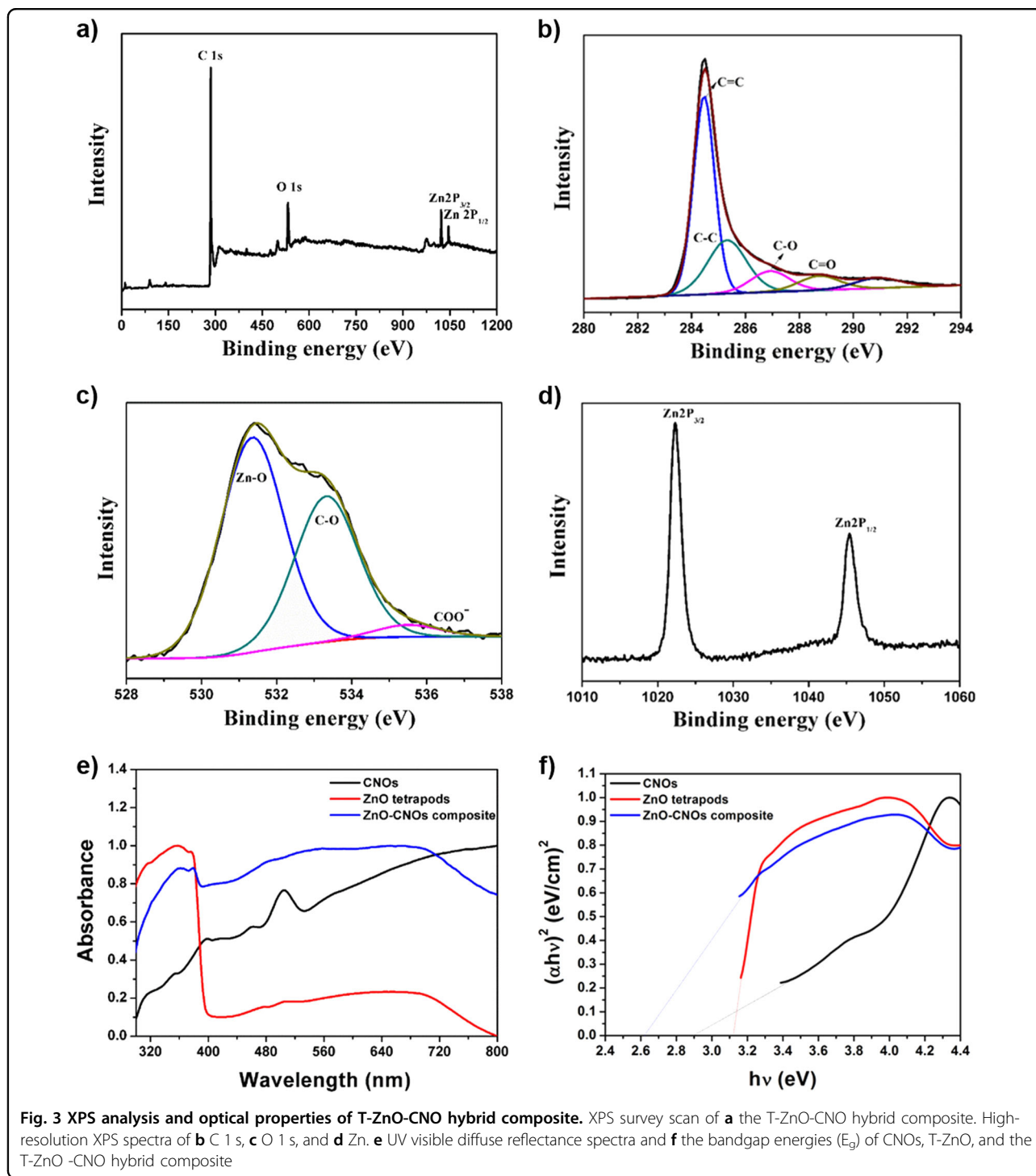
$2\theta = \sim 25^\circ$ and $2\theta = \sim 43^\circ$ corresponding to the (002) and (100) reflections of hexagonal graphitic carbon, respectively⁵². The characteristic diffraction peaks of T-ZnO (Fig. 2e) at 32° , 34.7° , 36.5° , 47.8° , 56.8° , 63° , 66.5° , 68.2° , 69.3° , and 77° are assigned to the (100), (002), (101), (102), (110), (103), (200), (112), (201), and (202) planes, respectively (JCPDS 01-089-7102)^{15,53}. The high peak intensity indicates the fabrication of pure T-ZnO with good crystallinity. After the decoration of CNOs, two new diffraction peaks at 25° and 43° are observed, as shown in Fig. 2f. Moreover, all the characteristic diffraction peaks of T-ZnO in the T-ZnO-CNOs composite are the same as those of T-ZnO, without other detectable impurity phases, indicating the high phase purity of the composite.

The XPS analysis was employed to characterize the chemical composition of the synthesized materials. The XPS survey spectra of CNOs and the T-ZnO-CNO 3D hybrid composite are shown in Fig. S2a and Fig. 3a, respectively. Fig. S2a reveals the existence of only C and O in the CNOs, with a C/O ratio of 4.66. The high-resolution C 1s spectrum of the CNOs shows four prominent peaks at 284.5 eV, 285.3 eV, 286.9 eV, and 288.8 eV indicating the existence of C=C, C-C, C-O, and C=O, respectively (Fig. S2b)³⁵. The deconvoluted O 1s spectrum of the CNOs presents two peaks at 531.9 eV and 533.4 eV corresponding to C=O and C-O, respectively (Fig. S2c)³⁵.

Figure 3a shows three distinct peaks indicating the existence of Zn, C, and O in the composite structure, thus, confirming the formation of the T-ZnO-CNO hybrid composite. The high-resolution C 1s spectrum (Fig. 3b) shows four deconvoluted peaks at 284.4 eV, 285.3 eV, 286.9 eV, and 288.7 eV assigned to C=C, C-C, C-O, and C=O respectively⁵⁴. The presence of C-O and C=O bonding peaks reveals the substantial decoration of CNOs on the surface of T-ZnO. The deconvoluted O 1s spectrum shown in Fig. 3c indicates three peaks at 531.3 eV, 533.3 eV, and 535.5 eV. The peak at 531.3 corresponds to the presence of characteristic Zn-O species⁵⁴. Whereas the peaks at 533.3 eV and 535.5 eV are assigned to C-O and COO⁻ bonding states, respectively. The high-resolution Zn 2p spectrum in Fig. 3d shows two symmetric peaks at 1022.3 eV and 1045.3 eV assigned to the Zn 2p_{3/2} and Zn 2p_{1/2}, respectively⁵⁴. The specific surface area was obtained by analyzing the N₂ adsorption-desorption isotherms of the T-ZnO-CNO hybrid composite. The specific surface area of the T-ZnO-CNO hybrid composite was calculated to be $\sim 43 \text{ m}^2 \text{ g}^{-1}$ (Fig. S2d).

UV-vis diffuse reflectance spectra

The optical properties of materials play a vital role in determining their photocatalytic activity. The UV-vis DRS were obtained to better understand the optical absorption



properties of the CNOs, T-ZnO, and the T-ZnO-CNO hybrid composite. The DRS spectra of the CNOs, T-ZnO, and the T-ZnO-CNO hybrid composite are shown in Fig. 3e. The CNOs and T-ZnO exhibit distinct absorption bands at ~ 505 nm and ~ 357 nm, respectively, which confirm the strong absorptions of the CNOs in the visible region and ZnO in the UV region³⁸. The charge transfer

in T-ZnO from the valence band (O 2p orbitals) to the conduction band (Zn 4s orbitals) is attributed to the intense absorption in the UV region¹⁷. In contrast to T-ZnO, the T-ZnO-CNO hybrid composite shows strong absorption over the entire visible region owing to the absorption of visible light by the CNOs. The charge density on specific C atoms induced by the surface

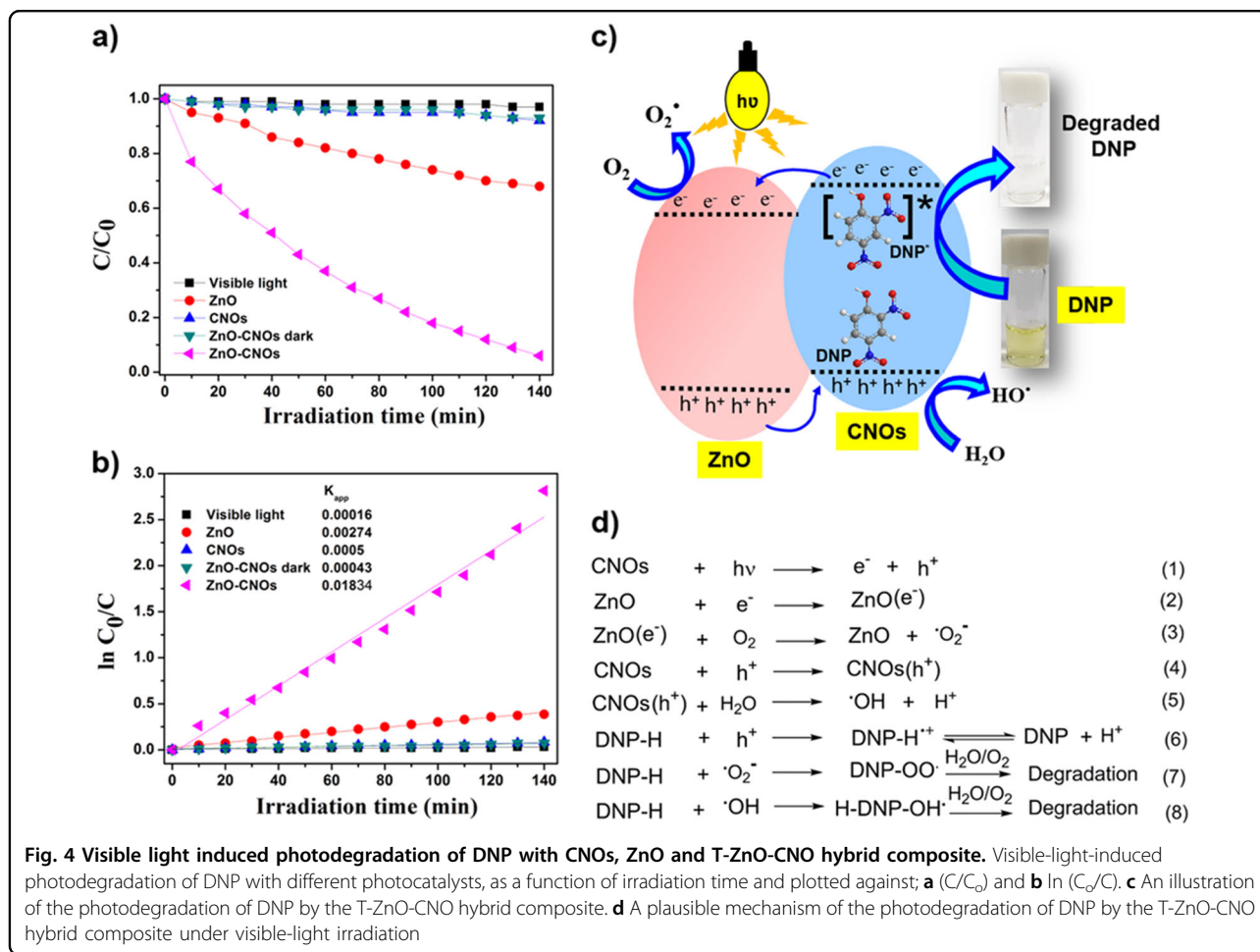
curvature and associated with surface defects, in the form of dangling bonds, significantly affects the photocatalytic activity of T-ZnO⁵⁵. Controlling the electronic state and adsorption characteristics of the T-ZnO with CNOs facilitates the absorption of visible light. The enhancement in the absorption intensity of the T-ZnO-CNO hybrid composite in the visible region is attributed to the enriched concentration of optically active centers, surface energy traps, and excitonic related recombination⁵⁵. Therefore, the decoration of CNOs on the surface of T-ZnO enhances the visible-light harvesting, which is a rather critical requirement for improving the photocatalytic performance. From the Tauc plots in Fig. 3f, the bandgaps of the CNOs, T-ZnO, and the T-ZnO-CNOs composite are observed to be 2.89 eV, 3.12 eV, and 2.62 eV, respectively, which are consistent with the results of earlier studies³⁸. The bandgap of the T-ZnO-CNO hybrid composite is lower than that of T-ZnO, indicating the more efficient utilization of visible light and the generation of more photoexcited carriers, and in turn, leading to a higher photocatalytic activity. It can be concluded that the decoration of CNOs on the surface of T-ZnO can considerably enhance the optical absorption, which is demonstrated by the improved photocatalytic degradation experiment below.

Photocatalytic degradation of DNP

The photocatalytic performance of the as-synthesized T-ZnO-CNO hybrid composite was assessed through the degradation of DNP. The direct photolysis of DNP from the blank experiment under visible-light irradiation could almost be neglected; moreover, the presence of the CNOs do not induce photocatalytic degradation (Fig. 4a). This indicates that the CNOs do not exhibit catalytic activity and that DNP is stable against visible-light-induced photolysis. The adsorption of DNP in the presence of the T-ZnO-CNO hybrid composite is negligible, as the degradation of DNP is not evident under the same experimental parameters in the absence of light, even after 140 min (Figs. 4a and S3c). Likewise, no significant change in the concentration of DNP is obtained, after 140 min in the absence of light with the CNOs and T-ZnO (Fig. S3a, b). In contrast, the concentration of DNP progressively decreases when irradiated with visible light (60 W tungsten lamp) in the presence of the T-ZnO-CNO hybrid composite. The intensity of the absorption peak at 358 nm decreases significantly with time and without a shift in the peak position (Fig. S3d). The peak position remains the same throughout the photocatalytic experiment without the emergence of any new absorption bands, indicating that no other chromophoric molecule is generated as a byproduct⁵⁶. The photodegradation efficiency of the T-ZnO-CNO hybrid composite is improved by ~92% over those of T-ZnO and the CNOs (Fig. 4b).

The rate constant of the T-ZnO-CNOs composite is ~7 times higher (0.01834 min^{-1}) than that of T-ZnO (0.00274 min^{-1}) and is ~36 times (0.0005 min^{-1}) higher than that of the CNOs (Fig. 4b). Table S1 compares the performances of the different materials in the degradation of DNP. The enhanced photocatalytic activity of the hybrid composite is attributed to the higher visible-light absorption, owing to the synergistic effect of the CNOs and T-ZnO, and the generation of diverse optically active centers. The strong interface between T-ZnO and the CNOs leads to the generation of a high density of surface traps for the effective absorption of reactive species and consequently enhances the active sites for catalysis²¹. The decoration of CNOs on the surface of T-ZnO is beneficial to increase the separation of photogenerated charge carriers²¹. Furthermore, the 3D morphology of T-ZnO augments the transport of photogenerated carriers owing to the presence of a direct electrical pathway. Moreover, the 3D morphology of ZnO increases the effective surface area and mass transfer of DNP.

A schematic of the possible photocatalytic mechanism of the T-ZnO-CNO hybrid composite under visible-light irradiation is presented in Fig. 4c. The DNP aqueous solution changes from light yellow to colorless, as observed in Fig. 4c. The overall steps involved in the photocatalytic degradation of DNP are shown in Fig. 4d. The CNOs can harvest visible light and act as photosensitizers owing to their strong absorption in the visible region. The CNOs and T-ZnO are activated by the absorption of visible light. Subsequently, the CNO electrons are quickly excited to the conduction band by the absorbed photons, and electron-hole pairs are generated (Eq. 1). The photoexcited electrons of the CNOs are rapidly transferred to the conduction band of T-ZnO (Eq. 2) and further captured by the surface-adsorbed oxygen to form superoxide radicals (O_2^-) (Eq. 3)⁵⁷. Simultaneously, to maintain electroneutrality, the photosensitized holes from T-ZnO are injected into the valence band of CNOs (Eq. 4). This process considerably retards the recombination of charge carriers and consequently enhances the photocatalytic activity. The photogenerated holes migrate to the surface of the photocatalyst and interact with the surface-adsorbed water molecules to generate hydroxyl radicals ($\cdot\text{OH}$)⁵⁸ (Eq. 5) or directly oxidize DNP molecules to organic radicals (Eq. 6). At the same time, the $\cdot\text{O}_2^-$ radicals generated by the surface-adsorbed oxygen, along with $\cdot\text{OH}$, are mainly responsible for the decomposition of DNP (Eqs. 7 and 8). Aerial oxygen acts as an electron scavenger to decompose the DNP into small molecules. The coupling of T-ZnO and the CNOs effectively shortens the diffusion path of photogenerated electron-hole pairs, facilitating the favorable migration of charge carriers and photoinduced reactive oxygen species (ROS). The active sites, in the form of

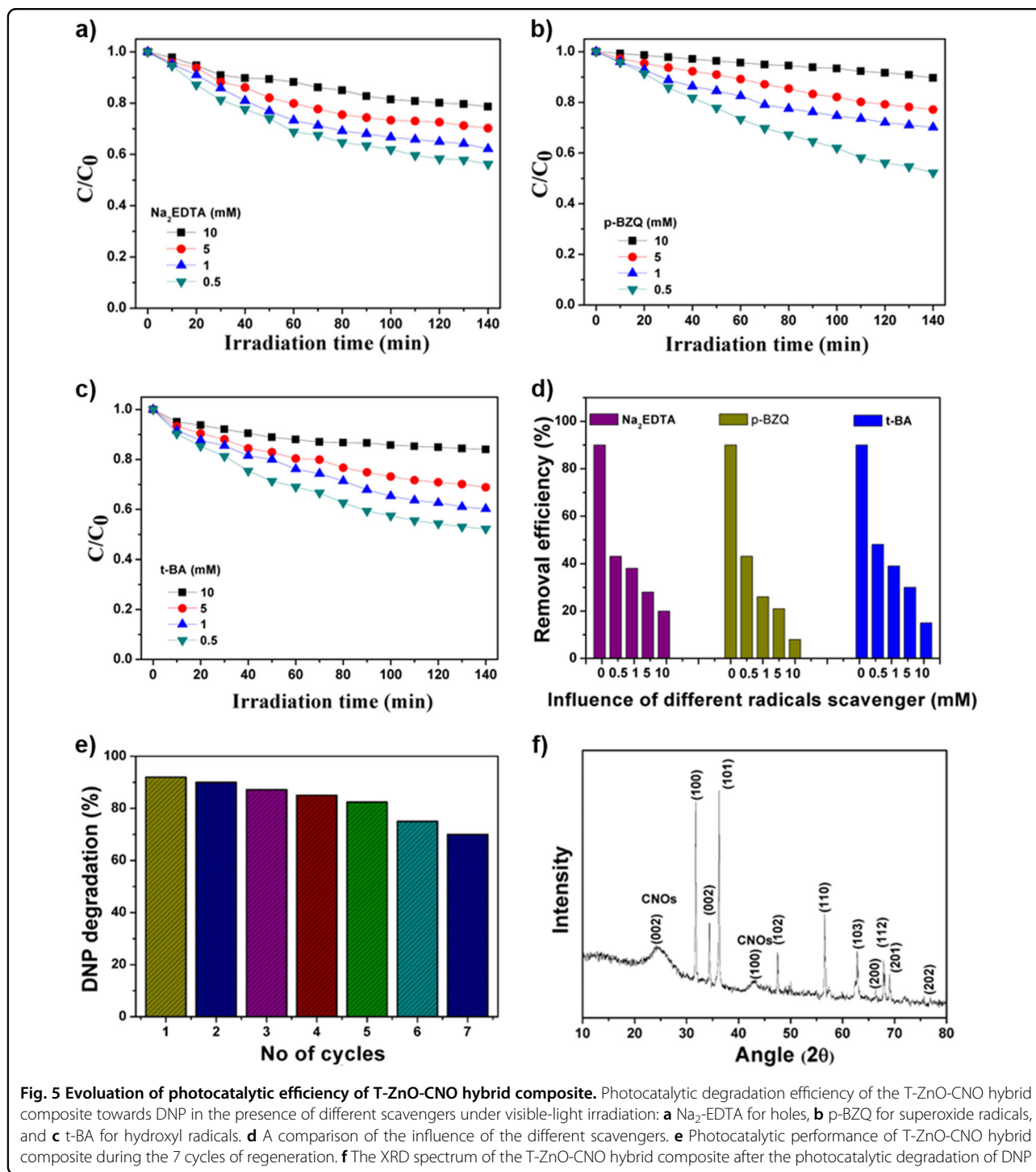


defects with unpaired electrons, significantly contribute to the activation of molecular oxygen via sequential electron transport to generate ROS. Furthermore, charge carrier separation and the generation of ROS, such as ·OH, ⁻O₂ and singlet oxygen (¹O₂), largely impact the photocatalytic degradation of organic pollutants⁵⁹. An efficient photocatalyst should promote the activation of molecular oxygen under visible-light irradiation to generate ROS and facilitate charge separation⁶⁰.

Active species trapping experiments were conducted for a deeper exploration of the major active radicals directly participating in the photodegradation of DNP and for an understanding of the photocatalytic mechanism of the T-ZnO-CNO hybrid composite. Three radical scavengers—Na₂-EDTA (h⁺ scavenger), t-BA (·OH scavenger), and p-BZQ, (⁻O₂ scavenger) in varying concentrations (0.5 mM, 1 mM, 5 mM, and 10 mM)—were introduced into the current system to evaluate the different influences on the photodegradation process. The existence of all the scavengers significantly oppressed the photocatalytic activity of the T-ZnO-CNO hybrid composite and consequently the degradation of DNP, as shown in Fig. 5a–c. The degradation efficiencies decrease

to ~20%, ~7%, and ~15% in the presence of Na₂-EDTA, p-BZQ, and t-BA, respectively, as shown in Fig. 5d. From the trapping experiments, it is revealed that the reactive oxygen species ⁻O₂ is the most active initiator of the photocatalytic degradation of DNP, while ·OH and h⁺ are secondary reactive species. The enhanced photocatalytic efficiency of T-ZnO after decoration with the CNOs is attributed to the enhanced charge transfer and robust generation of ROS. Profiting from the structural advantage brought by the decoration of the CNOs on the surface of T-ZnO, a significant enhancement in surface traps for the adsorption of active species and DNP molecules is observed.

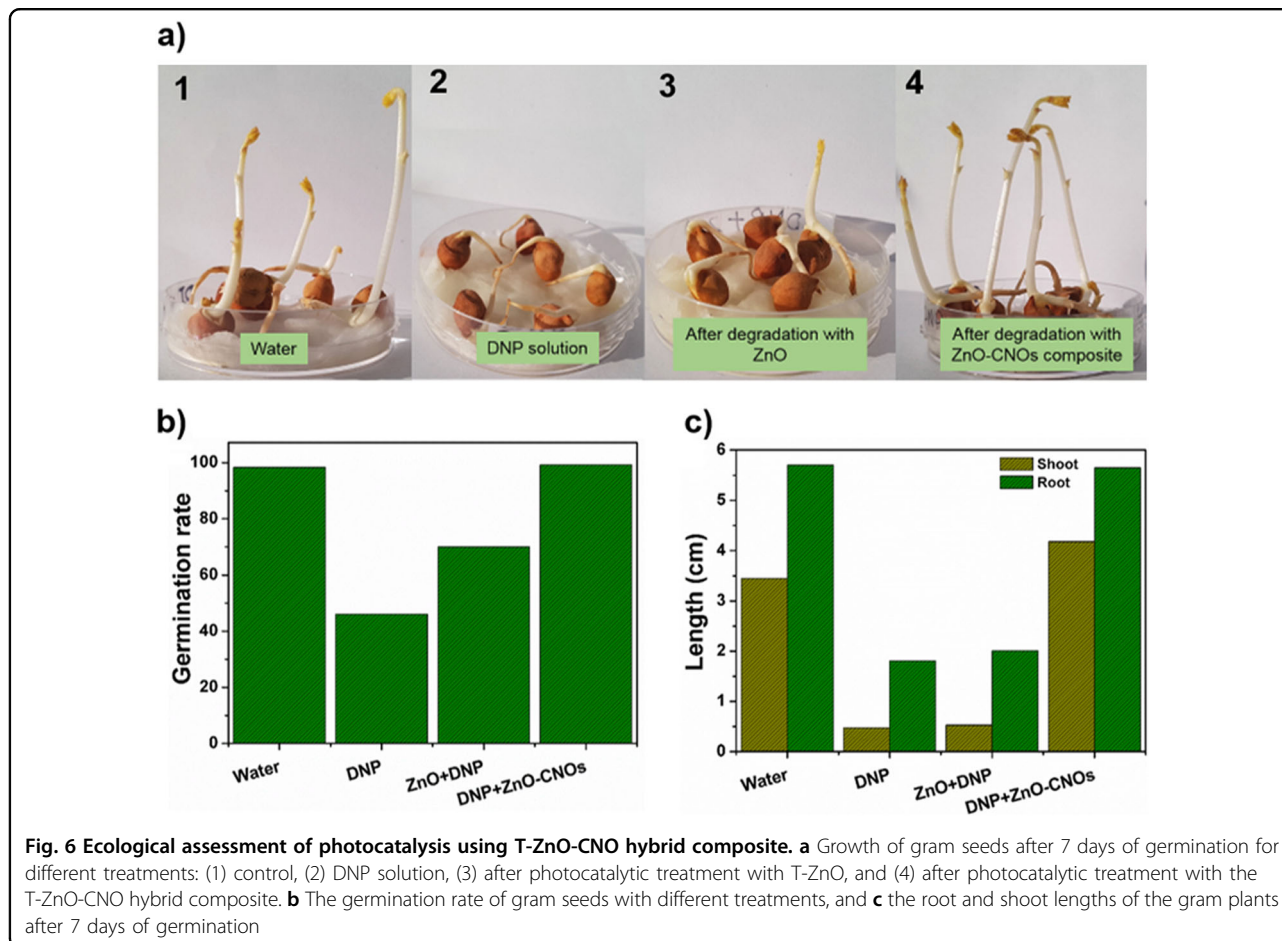
The regeneration of a photocatalyst is a necessary step towards commercial adaptation. The photocatalytic degradation of DNP using the T-ZnO-CNO hybrid composite was repeated seven times to confirm the recyclability and stability of the photocatalyst. The composite was recycled via centrifugation, washed with DI water, and subsequently dried at 80 °C overnight. After five cycles, there is a slight decrease in the degradation of DNP, which might be derived from the loss of the T-ZnO-CNO hybrid composite (Fig. 5e). Consequently, the good



recyclability of the T-ZnO-CNOs composite renders it an effective visible-light photocatalyst for commercial applications. Additionally, the XRD pattern of the T-ZnO-CNOs composite was analyzed before and after the photocatalytic experiments. Figure 5f shows that there is no apparent change in the diffraction peaks before and after the degradation of DNP, which reveals the stability of the composite material during the photocatalytic reactions.

Assessment of phytotoxicity

The impact of the DNP solution after photodegradation towards the ecological assessment was analyzed to evaluate the possible use of the post-treated samples. Moreover, this practice can achieve the safer reuse of treated water. The phytotoxicity of the DNP solution before and after treatment with the photocatalyst along with a blank sample is demonstrated in Fig. 6a. To compare the effect



of the DNP solution, before and after the photocatalytic degradation, on the germination and growth of the roots and shoots of gram plants, four different sets of seeds were used: The first set of seeds were germinated in DI water (control); the DNP solution was used for the germination of the second set of seeds; in the third set, the DNP solution after degradation using T-ZnO was used for the germination of seeds; and the DNP solution after photodegradation with the T-ZnO-CNO hybrid composite was used for the germination of the fourth set of seeds. The root lengths, shoot lengths, and germination rates were monitored after the seventh day of germination. The DNP solution before degradation results in the strong inhibition of the germination of common gram seeds, indicating the highly toxic nature of DNP (Fig. 6a2). The DNP solution treated with only T-ZnO also inhibits seed germination in contrast to the seeds of the control set (Fig. 6a1, a3), indicating the phytotoxicity of the solution owing to incomplete degradation of DNP. The DNP solution treated with the T-ZnO-CNO hybrid composite under visible-light irradiation does not have any adverse effects on the seed germination, reflecting the nontoxicity of the treated water (Fig. 6a4). Significantly, a slight increase in the germination rate (99%) is observed

for the solution treated with the T-ZnO-CNO hybrid composite compared with that of the control (98%), as shown in Fig. 6b. Furthermore, the germination rate for the T-ZnO-treated water (70%) is higher than that of the DNP solution (46%) (Fig. 6b). These results reveal that the T-ZnO-CNO hybrid composite can efficiently degrade the DNP into nontoxic products.

We observe an enhancement in the shoot lengths of the gram plants treated with the DNP solution after photocatalytic degradation by the T-ZnO-CNO hybrid composite compared with those of the control, whereas no apparent change in the root lengths is observed (Fig. 6c). The seedling length suppression is prominent for both the DNP solution and the T-ZnO-treated DNP solution, as shown in Fig. 6c. The results suggest the ecological safety of the T-ZnO-CNO hybrid composite for the photocatalytic degradation of pollutants.

Conclusions

A visible-light-sensitive hybrid composite of T-ZnO and CNOs was fabricated via a facile one-step process, which offers easy accessibility of the characteristic features of both constituents. The inherent properties of T-ZnO and the CNOs complement each other and consequently lead

to enhanced photocatalytic properties, even in the visible region. The T-ZnO-CNO hybrid composite exhibits an augmented photocatalytic degradation of DNP under visible-light irradiation, achieving a degradation of 92% within 140 min. The increased photocatalytic activity could be attributed to the considerable enhancement in the visible-light absorption owing to the synergistic effect of CNOs sensitization and the construction of a hetero-junction structure with a unique tetrapod morphology, leading to a high charge-separation efficiency. A plausible photocatalysis mechanism is proposed based on trapping tests and bandgap measurements. Moreover, the DNP solution treated with the T-ZnO-CNO hybrid composite under visible-light irradiation is nontoxic to plants, indicating the ecological safety of the material. The T-ZnO-CNO composite can provide insights into the design of advanced materials and technologies.

Acknowledgements

This research was supported by the R&D Convergence Program of MSIP (Ministry of Science, ICT and Future Planning) and NST (National Research Council of Science & Technology) of the Republic of Korea (Grant CAP-13-02-ETRI). This research was supported by the Nano Material Technology Development Program through the National Research Foundation of Korea (NRF), funded by the Ministry of Science, ICT and Future Planning (NRF-2016M3A7B4027712). This research was supported by the Basic Science Research Program through the NRF, funded by the Ministry of Education (NRF-2016R1D1A1B01008736). The Kiel authors thank Deutsche Forschungsgemeinschaft for financial support under GRK 2154 (P3) scheme.

Conflict of interest

The authors declare no conflict of interest.

Publisher's note

Springer Nature remains neutral with regard to jurisdictional claims in published maps and institutional affiliations.

Supplementary information is available for this paper at <https://doi.org/10.1038/s41427-019-0107-0>.

Received: 29 August 2018 Revised: 16 November 2018 Accepted: 26 November 2018.

Published online: 13 February 2019

References

- Scott-Fordsmand, J. J., Navas, J. M., Hund-Rinke, K., Nowack, B. & Amorim, M. J. B. Nanomaterials to microplastics: swings and roundabouts. *Nano Today* **17**, 7–10 (2017).
- Darabdhara, G. et al. Reduced graphene oxide nanosheets decorated with Au-Pd bimetallic alloy nanoparticles towards efficient photocatalytic degradation of phenolic compounds in water. *Nanoscale* **8**, 8276–8287 (2016).
- Shetty, D. et al. Porous polycalix[4]arenes for fast and efficient removal of organic micropollutants from water. *ACS Appl. Mater. Interfaces* **10**, 2976–2981 (2018).
- Ma, H.-Y., Zhao, L., Wang, D.-B., Zhang, H. & Guo, L.-H. Dynamic tracking of highly toxic intermediates in photocatalytic degradation of pentachlorophenol by continuous flow chemiluminescence. *Environ. Sci. Technol.* **52**, 2870–2877 (2018).
- Ahmad, R. & Hasan, I. Efficient remediation of an aquatic environment contaminated by Cr(VI) and 2,4-dinitrophenol by XG-g-polyaniline@ZnO nano-composite. *J. Chem. Eng. Data* **62**, 1594–1607 (2017).
- Cao, X., Oda, Y. & Shiraiishi, F. Photocatalytic and adsorptive treatment of 2,4-dinitrophenol using a TiO₂ film covering activated carbon surface. *Chem. Eng. J.* **156**, 98–105 (2010).
- Zhang, Y. et al. Superhydrophobic nanoporous polymers as efficient adsorbents for organic compounds. *Nano Today* **4**, 135–142 (2009).
- Dias, E. M. & Petit, C. Towards the use of metal-organic frameworks for water reuse: a review of the recent advances in the field of organic pollutants removal and degradation and the next steps in the field. *J. Mater. Chem. A* **3**, 22484–22506 (2015).
- Kim, S., Piao, G., Han, D. S., Shon, H. K. & Park, H. Solar desalination coupled with water remediation and molecular hydrogen production: a novel solar water-energy nexus. *Energy Environ. Sci.* **11**, 344–353 (2018).
- Huang, H., Xiao, K., Zhang, T., Dong, F. & Zhang, Y. Rational design on 3D hierarchical bismuth oxyiodides *via in situ* self-template phase transformation and phase-junction construction for optimizing photocatalysis against diverse contaminants. *Appl. Catal. B-Environ.* **203**, 879–888 (2017).
- Huang, H. et al. In situ assembly of BiO@Bi₂O₃/C₁₂p-n junction: charge induced unique front-lateral surfaces coupling heterostructure with high exposure of BiO{001} active facets for robust and nonselective photocatalysis. *Appl. Catal. B-Environ.* **199**, 75–86 (2016).
- Yang, S.-F. et al. SrTiO₃ nanocubes decorated with Ag/AgCl nanoparticles as photocatalysts with enhanced visible-light photocatalytic activity towards the degradation of dyes, phenol and bisphenol A. *Environ. Sci. Nano* **4**, 585–595 (2017).
- Huang, H., He, Y., Du, X., Chu, P. K. & Zhang, Y. A general and facile approach to heterostructured core/shell BiVO₄/BiO p-n junction: Room-temperature *in situ* assembly and highly boosted visible-light photocatalysis. *ACS Sustain. Chem. Eng.* **3**, 3262–3273 (2015).
- Bacsa, R. R. et al. Synthesis and structure–property correlation in shape-controlled ZnO nanoparticles prepared by chemical vapor synthesis and their application in dye-sensitized solar cells. *Adv. Funct. Mater.* **19**, 875–886 (2009).
- Mishra, Y. K. & Adelung, R. ZnO tetrapod materials for functional applications. *Mater. Today* **21**, 631–651 (2018).
- Peng, Y.-K. & Tsang, S. C. E. Facet-dependent photocatalysis of nanosize semiconductive metal oxides and progress of their characterization. *Nano Today* **18**, 15–34 (2018).
- Tao, S., Yang, M., Chen, H., Zhao, S. & Chen, G. Continuous synthesis of Ag/AgCl/ZnO composites using flow chemistry and photocatalytic application. *Ind. Eng. Chem. Res.* **57**, 3263–3273 (2018).
- Li, M. et al. Nature-derived approach to oxygen and chlorine dual-vacancies for efficient photocatalysis and photoelectrochemistry. *ACS Sustain. Chem. Eng.* **6**, 2395–2406 (2018).
- Gröttrup, J. et al. Porous ceramics based on hybrid inorganic tetrapodal networks for efficient photocatalysis and water purification. *Ceram. Int.* **43**, 14915–14922 (2017).
- Gröttrup, J. et al. Three-dimensional flexible ceramics based on interconnected network of highly porous pure and metal alloyed ZnO tetrapods. *Ceram. Int.* **42**, 8664–8676 (2016).
- Bipin Kumar, G., Vaneet, G., Govind, G. & Shanker, V. Highly efficient luminescence from hybrid structures of ZnO/multi-walled carbon nanotubes for high performance display applications. *Nanotechnology* **21**, 475701 (2010).
- Begum, A., Tripathi, K. M. & Sarkar, S. Water-induced formation, characterization, and photoluminescence of carbon nanotube-based composites of gadolinium(III) and platinum(II) dithiolenes. *Chem. Eur. J.* **20**, 16657–16661 (2014).
- Tripathi, K. M., Begum, A., Sonkar, S. K. & Sarkar, S. Nanospheres of copper(III) 1,2-dicarbomethoxy-1,2-dithiolate and its composite with water soluble carbon nanotubes. *New J. Chem.* **37**, 2708–2715 (2013).
- Su, D. S., Perathoner, S. & Centi, G. Nanocarbons for the development of advanced catalysts. *Chem. Rev.* **113**, 5782–5816 (2013).
- Han, M. et al. Recent progress on the photocatalysis of carbon dots: classification, mechanism and applications. *Nano Today* **19**, 201–218 (2018).
- Kong, J. et al. Boosting interfacial interaction in hierarchical core-shell nanostructure for highly effective visible photocatalytic performance. *J. Phys. Chem. C* **122**, 6137–6143 (2018).
- Huang, H. et al. Fabrication of multiple heterojunctions with tunable visible-light-active photocatalytic reactivity in BiOBr–BiOI full-range composites based on microstructure modulation and band structures. *ACS Appl. Mater. Interfaces* **7**, 482–492 (2015).

28. Boi, F. S., Ivaturi, S., Wang, S. & Zhang, X. Temperature driven structural transitions in the graphitic-arrangement of carbon onions filled with FePd₃ nano crystals. *Carbon* **120**, 392–396 (2017).
29. Tang, H. et al. Revealing the formation mechanism of ultrahard nanotwinned diamond from onion carbon. *Carbon N. Y.* **129**, 159–167 (2018).
30. Dubey, P., Tripathi, K. M. & Sonkar, S. K. Gram scale synthesis of green fluorescent water-soluble onion-like carbon nanoparticles from camphor and polystyrene foam. *RSC Adv.* **4**, 5838–5844 (2014).
31. Berman, D. et al. Operando tribochemical formation of onion-like-carbon leads to macroscale superlubricity. *Nat. Commun.* **9**, 1164 (2018).
32. Amora, M. et al. Biocompatibility and biodistribution of functionalized carbon nano-onions (F-CNOs) in a vertebrate model. *Sci. Rep.* **6**, 33923 (2016).
33. Keller, N. et al. The catalytic use of onion-like carbon materials for styrene synthesis by oxidative dehydrogenation of ethylbenzene. *Angew. Chem. Int. Ed.* **41**, 1885–1888 (2002).
34. Tripathi, K. M. et al. From the traditional way of pyrolysis to tunable photoluminescent water soluble carbon nano-onions for cell imaging and selective sensing of glucose. *RSC Adv.* **6**, 37319–37329 (2016).
35. Tripathi, K. M., Tran, T. S., Kim, Y. J. & Kim, T. Green fluorescent onion-like carbon nanoparticles from flaxseed oil for visible light induced photocatalytic applications and label-free detection of Al(III) ions. *ACS Sustain. Chem. Eng.* **5**, 3982–3992 (2017).
36. Shi, L., Wang, F., Zhang, J. & Sun, J. Onion-like carbon modified porous graphitic carbon nitride with excellent photocatalytic activities under visible light. *Ceram. Int.* **42**, 18116–18123 (2016).
37. Singh, A. et al. Pollutant soot for pollutant dye degradation: soluble graphene nanosheets for visible light induced photodegradation of methylene blue. *ACS Sustain. Chem. Eng.* **5**, 8860–8869 (2017).
38. Khare, P. et al. Sunlight-induced selective photocatalytic degradation of methylene blue in bacterial culture by pollutant soot derived nontoxic graphene nanosheets. *ACS Sustain. Chem. Eng.* **6**, 579–589 (2018).
39. Tripathi, K. M. et al. Large-scale synthesis of soluble graphitic hollow carbon nanorods with tunable photoluminescence for the selective fluorescent detection of DNA. *New J. Chem.* **40**, 1571–1579 (2016).
40. Tripathi, K. M. et al. Green carbon nanostructured quantum resistive sensors to detect volatile biomarkers. *Sustain. Mater. Technol.* **16**, 1–11 (2018).
41. Mishra, Y. K. et al. Direct growth of freestanding ZnO tetrapod networks for multifunctional applications in photocatalysis, uv photodetection, and gas sensing. *ACS Appl. Mater. Interfaces* **7**, 14303–14316 (2015).
42. Mishra, Y. K. et al. Fabrication of macroscopically flexible and highly porous 3d semiconductor networks from interpenetrating nanostructures by a simple flame transport approach. *Part. Part. Syst. Charact.* **30**, 775–783 (2013).
43. Sharma, M. et al. ZnO tetrapods and activated carbon based hybrid composite: adsorbents for enhanced decontamination of hexavalent chromium from aqueous solution. *Chem. Eng. J.* **358**, 540–551 (2019).
44. Bhati, A., Singh, A., Tripathi, K. M. & Sonkar, S. K. Sunlight-induced photochemical degradation of methylene blue by water-soluble carbon nanorods. *Int. J. Photoenergy* **2016**, 8 (2016).
45. Sonkar, S. K., Roy, M., Babar, D. G. & Sarkar, S. Water soluble carbon nano-onions from wood wool as growth promoters for gram plants. *Nanoscale* **4**, 7670–7675 (2012).
46. Bhati, A. et al. Exploration of nano carbons in relevance to plant systems. *New J. Chem.* **42**, 16411–16427 (2018).
47. Tripathi, K. M. et al. Sustainable changes in the contents of metallic micronutrients in first generation gram seeds imposed by carbon nano-onions: life cycle seed to seed study. *ACS Sustain. Chem. Eng.* **5**, 2906–2916 (2017).
48. Fen, T. S. et al. Nanoparticle interactions guided by shape-dependent hydrophobic forces. *Adv. Mater.* **30**, 1707077 (2018).
49. Feng, X. et al. Reversible super-hydrophobicity to super-hydrophilicity transition of aligned ZnO nanorod films. *J. Am. Chem. Soc.* **126**, 62–63 (2004).
50. Tripathi, K. M., Singh, A., Bhati, A., Sarkar, S. & Sonkar, S. K. Sustainable feasibility of the environmental pollutant soot to few-layer photoluminescent graphene nanosheets for multifunctional applications. *ACS Sustain. Chem. Eng.* **4**, 6399–6408 (2016).
51. Tripathi, K. M., Tran, T. S., Tung, T. T., Losic, D. & Kim, T. Water soluble fluorescent carbon nanodots from biosource for cells imaging. *J. Nanomater.* **2017**, 10 (2017).
52. Liu, Y., Vander Wal, R. L. & Khabashesku, V. N. Functionalization of carbon nano-onions by direct fluorination. *Chem. Mater.* **19**, 778–786 (2007).
53. Gedamu, D. et al. Rapid fabrication technique for interpenetrated ZnO nanotetrapod networks for fast uv sensors. *Adv. Mater.* **26**, 1541–1550 (2014).
54. Kim, C. H. & Kim, B.-H. Zinc oxide/activated carbon nanofiber composites for high-performance supercapacitor electrodes. *J. Power Sources* **274**, 512–520 (2015).
55. Smazna, D. et al. Buckminsterfullerene hybridized zinc oxide tetrapods: defects and charge transfer induced optical and electrical response. *Nanoscale* **10**, 10050–10062 (2018).
56. Deng, W. et al. Visible-light-driven photocatalytic degradation of organic water pollutants promoted by sulfite addition. *Environ. Sci. Technol.* **51**, 13372–13379 (2017).
57. Huang, H. et al. Macroscopic polarization enhancement promoting photo- and piezoelectric-induced charge separation and molecular oxygen activation. *Angew. Chem. Int. Ed.* **56**, 11860–11864 (2017).
58. Huang, H. et al. Anionic group self-doping as a promising strategy: Band-gap engineering and multi-functional applications of high-performance CO₃²⁻-Doped Bi₂O₂CO₃. *ACS Catal.* **5**, 4094–4103 (2015).
59. Huang, H. et al. Visible-light-responsive sillén-structured mixed-cationic CdBiO₃Br nanosheets: layer structure design promoting charge separation and oxygen activation reactions. *J. Phys. Chem. C* **122**, 2661–2672 (2018).
60. Huang, H. et al. Bi₂O₂(OH)(NO₃) as a desirable [Bi₂O²⁺]₂ layered photocatalyst: strong intrinsic polarity, rational band structure and {001} active facets co-beneficial for robust photooxidation capability. *J. Mater. Chem. A* **3**, 24547–24556 (2015).